

See discussions, stats, and author profiles for this publication at: <https://www.researchgate.net/publication/263939534>

Direct Evidence of Lithium-Induced Atomic Ordering in Amorphous TiO₂ Nanotubes

ARTICLE *in* CHEMISTRY OF MATERIALS · FEBRUARY 2014

Impact Factor: 8.35 · DOI: 10.1021/cm403951b

CITATIONS

21

READS

72

7 AUTHORS, INCLUDING:



Meng Gu

University of California, Davis

69 PUBLICATIONS 1,318 CITATIONS

SEE PROFILE



Anmin Nie

Michigan Technological University

37 PUBLICATIONS 253 CITATIONS

SEE PROFILE



Gregory M. Odegard

Michigan Technological University

114 PUBLICATIONS 2,704 CITATIONS

SEE PROFILE

Direct Evidence of Lithium-Induced Atomic Ordering in Amorphous TiO₂ Nanotubes

Qi Gao,^{†,⊥} Meng Gu,^{‡,⊥} Anmin Nie,^{†,§,⊥} Farzad Mashayek,^{||} Chongmin Wang,^{*,‡} Gregory M. Odegard,[†] and Reza Shahbazian-Yassar^{*,†,§,||}

[†]Department of Mechanical Engineering-Engineering Mechanics, Michigan Technological University, Houghton, Michigan 49931, United States

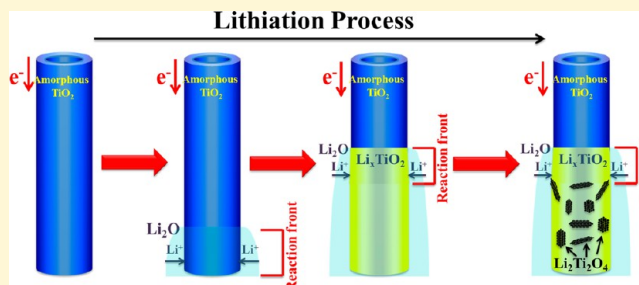
[‡]Environmental Molecular Sciences Laboratory, Pacific Northwest National Laboratory, Richland, Washington 99352, United States

[§]Department of Physics and ^{||}Department of Mechanical and Industrial Engineering, University of Illinois at Chicago, Chicago, Illinois 60607, United States

S Supporting Information

ABSTRACT: In this paper, we report the first direct chemical and imaging evidence of lithium-induced atomic ordering in amorphous TiO₂ nanomaterials and propose new reaction mechanisms that contradict the many works in the published literature on the lithiation behavior of these materials. The lithiation process was conducted in situ inside an atomic resolution transmission electron microscope. Our results indicate that the lithiation started with the valence reduction of Ti⁴⁺ to Ti³⁺ leading to a Li_xTiO₂ intercalation compound. The continued intercalation of Li ions in TiO₂ nanotubes triggered an amorphous to crystalline phase transformation.

The crystals were formed as nano-islands and identified to be Li₂Ti₂O₄ with cubic structure ($a = 8.375 \text{ \AA}$). The tendency for the formation of these crystals was verified with density functional theory (DFT) simulations. The size of the crystalline islands provides a characteristic length scale ($\sim 5 \text{ nm}$) at which the atomic bonding configuration has been changed within a short time period. This phase transformation is associated with local inhomogeneities in Li distribution. On the basis of these observations, a new reaction mechanism is proposed to explain the first cycle lithiation behavior in amorphous TiO₂ nanotubes.



INTRODUCTION

The next generation of Li ion batteries (LIB) has drawn much interest because of their applications in hybrid electric vehicles (HEVs),¹ plug-in hybrid electric vehicles (PHEVs),² and other electric utilities. Graphite is a widely used anode material in commercial LIB. However, graphite has several drawbacks such as low theoretical capacity and capacity fading.³ To circumvent these problems, several new materials have been developed to replace the graphite, including Si,⁴ Sn,⁵ Co₃O₄,⁶ and Ge.⁷ However, a major limitation of these alternatives is that they experience large volume changes in the first cycle, leading to cracking, fracture, and in turn, capacity fading and failure of batteries.

In recent years, nanotubular structures of TiO₂-based materials with larger specific surface area, shorter diffusion length, and faster kinetics of electrochemical reactions have been considered to be a viable alternative to graphite electrodes due to their stable capacity retention and safe operation during intercalation.^{3,8,9} TiO₂ has almost the same theoretical capacity ($\sim 336 \text{ mAh/g}$) as that of commercial-grade graphite ($\sim 372 \text{ mAh/g}$), but the volume expansion is less than 3%.¹⁰ In addition, the operation voltage of TiO₂ is as high as 1.7 V (Li/Li⁺ redox couple) compared with that of graphite (0.1 V). The

higher operation voltage results in safer battery operation with lower self-discharge and good capacity retention during cycling.¹¹ This property will make TiO₂ to be compatible with several novel cathode materials of LiCoPO₄¹² and LiCo_{0.5}Mn_{1.5}O₄¹³ to achieve high performance Li-ion batteries.

Interestingly, in spite of extensive ex situ electrochemical testing on TiO₂ nanotubes,^{14–19} no direct TEM evidence on their lithiation behavior has been reported. The in situ electrochemical lithiation study in TEM allows direct observation of morphological and chemical evolution in real time. The authors²⁰ and Huang et al.²¹ pioneered the concept of an “open-cell” design to study the electrochemical behavior of battery electrode materials. This cell is made of a single nanowire as anode, ionic liquid, or solid Li₂O as electrolyte, and LiCoO₂ or lithium metal as cathode. This method of observation can provide atomic-level spatial resolution and analytical capability to study Li ion insertion mechanisms into electrode materials during the lithiation/delithiation cycle.^{20,22–25} Since its invention, this technique has revealed

Received: November 30, 2013

Revised: January 20, 2014

Published: January 27, 2014

many details about the lithiation mechanisms in Si,^{22,23,26–31} Ge,³² Al₂O₃,³³ SnO₂,^{21,25,34–36} ZnO,³⁷ graphene,³⁸ and carbon nanotubes³⁹ that were unknown to the Li-ion battery community.

In the present work, for the first time, in situ studies of electrochemical lithiation of amorphous TiO₂ nanotubes (a-TNTs) inside high-resolution TEM will be reported. Electron energy loss spectroscopy (EELS) was also conducted to better understand the changes in chemical and electronic properties. The finding of this study provides the first direct insight into the details of lithiation mechanism, chemical, structural, and electronic evolution for a-TNTs as anode materials. High resolution TEM (HRTEM) analysis revealed the formation of crystalline islands of Li₂Ti₂O₄ in the lithiated amorphous matrix. These findings were verified with density functional theory (DFT) simulations.

EXPERIMENTAL SECTION

TiO₂ Nanotube Synthesis. The TiO₂ nanotubes were grown by the anodization setup. Titanium foil (Sigma-Aldrich, 0.25 mm thick, 99.99%) was used as the substrate for growth of the oxide nanotube arrays. The foils were sonicated in the sequence of ethanol, deionized water, and acetone for 10 min each. Titanium foils served as the anodic electrode while platinum was used as the cathodic electrode. Electrolyte used in the experiment was 0.2 wt % NH₄F solution in a plastic beaker, which was prepared by NH₄F crystals, ethylene glycol, and deionized water with the ratio of 49:1 that helped dissolve the NH₄F crystals. The anodization process was conducted at the voltage of 40 V for the processing time of 8 h at room temperature. Upon completion of the anodization, the titanium foils were rinsed with deionized water and dried in the atmosphere. The products were characterized by a field emission scanning electron microscopy (FE-SEM) (Hitachi S-4700, Japan) under the operating voltage of 10 kV.

In Situ TEM Setup. The TiO₂ nanotubes with the substrate of titanium foil were treated with ethanol for one day and air-dried for two days. The nanotubes were scratched off from the film and then glued to a tungsten (W) tip with conductive epoxy. Lithium metal was scratched by a gold (Au) wire inside the glovebox and transferred by a sealed container with Ar gas. The W and Au wires were mounted on the stationary and piezo-movable sides of an in situ scanning tunneling microscope (STM) that operated inside a TEM, respectively. The naturally grown Li₂O layer on the Li metal worked as a solid electrolyte. The Li₂O/Li electrode side was moved forward to contact one of the TiO₂ nanotubes. Once a reliable electrical contact was built, a potential ranging from −2 to −4 V was applied to the TiO₂ nanotubes to initiate the lithiation. The in situ TEM experiments were performed using an aberration-corrected scanning transmission electron microscope (ARM 200CF, JEOL, Japan) as well as a high resolution TEM (JEOL4000FX) operated at 200 keV.

The EELS signals were acquired using a Gatan Image Filter (Quantum 965, GATAN, USA) with a 2k × 2k pixels CCD camera, which allows simultaneous acquisition of the low loss and high loss region. The EELS studies were conducted in the scanning transmission electron microscopy (STEM) mode on a Titan 80-300 (FEI, USA) operated at 300 keV with an energy dispersion of 0.25 eV/channel and an energy resolution of ~0.9 eV.

RESULTS AND DISCUSSION

The in situ lithiation setup where Li metal with Li₂O is placed on the gold wire and a-TNTs are attached to the STM tip is shown in Figure S1 (Supporting Information). Using a piezo-driven stage with nanometer precision, the Li/Li₂O was moved toward individual nanotubes. Once a reliable contact was made, the bias voltage of −3 V was applied to the nanotubes to trigger the lithiation process.

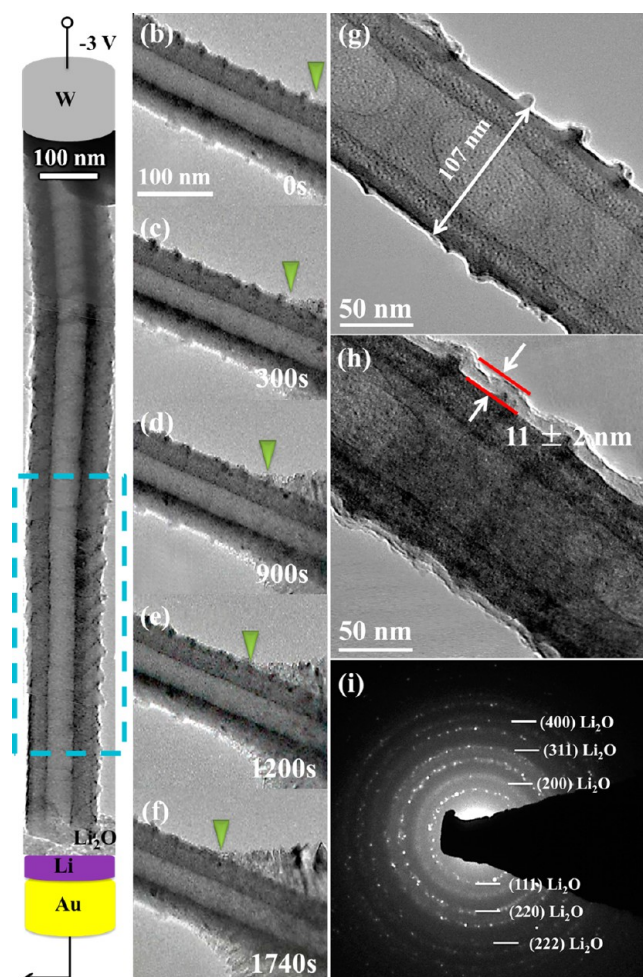


Figure 1. Serial snapshot images of the lithiation process for an individual a-TNT. (a) The whole structural view of a selected a-TNT with diameter of around 130 nm. (b–f) A selected area of lithiation process monitored from the reference 0 s (b) to 1740 s (f). The evolution of Li₂O layer formation is observed on the surface of the nanotube as marked by the green arrow. The HRTEM images of Li₂O layer formation on the surface of an individual a-TNT are shown as (g–i). (g) A pristine TiO₂ nanotube with diameter of 107 nm. (h) A thickness of 11 ± 2 nm layer formation on the lithiated nanotube. (i) Corresponding diffraction pattern of the Li₂O layer.

Figure 1a–f illustrates the lithiation process of an a-TNT in real time. When the free-end of the a-TNT contacted with Li₂O, the lithiation process started (under the applied voltage of −3 V) with the formation of a layer on the surface of the a-TNT. The progress of this surface layer as a function of time is marked by a blue dotted square.

In order to better understand the structure of this surface layer, HRTEM images of nanotubes before and after lithiation were compared. Figure 1g shows a pristine a-TNT with the diameter of 107 nm. After lithiation, a layer was formed on the surface of the nanotube. The thickness of this layer was estimated to be 11 ± 2 nm as marked by the white arrows in Figure 1h. A selected area electron diffraction (SAED) pattern was recorded on the layer as shown in Figure 1i. The indexed (111), (220), and (311) planes correspond to Li₂O phase indicating that the surface layer is made of polycrystalline Li₂O.

The formation of the Li₂O layer observed on the surface of TiO₂ nanotubes during lithiation can be explained knowing that Li ions can react with the residual oxygen in the TEM chamber

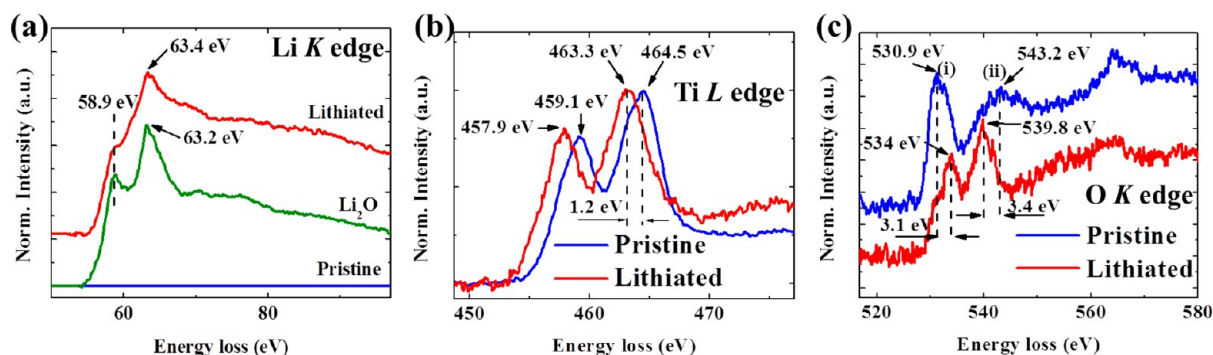


Figure 2. EELS spectra of the Li K edge, Ti L edge, and O K edge taken from the selected area of the nanotube before and after lithiation. (a) The EELS spectra show Li K edge of pristine, lithiated TiO₂ nanotube, and Li₂O as a reference. (b) A comparison between Ti L edge in pristine and lithiated TiO₂ nanotubes is shown. (c) Showing O K edge in pristine and lithiated TiO₂ nanotubes.

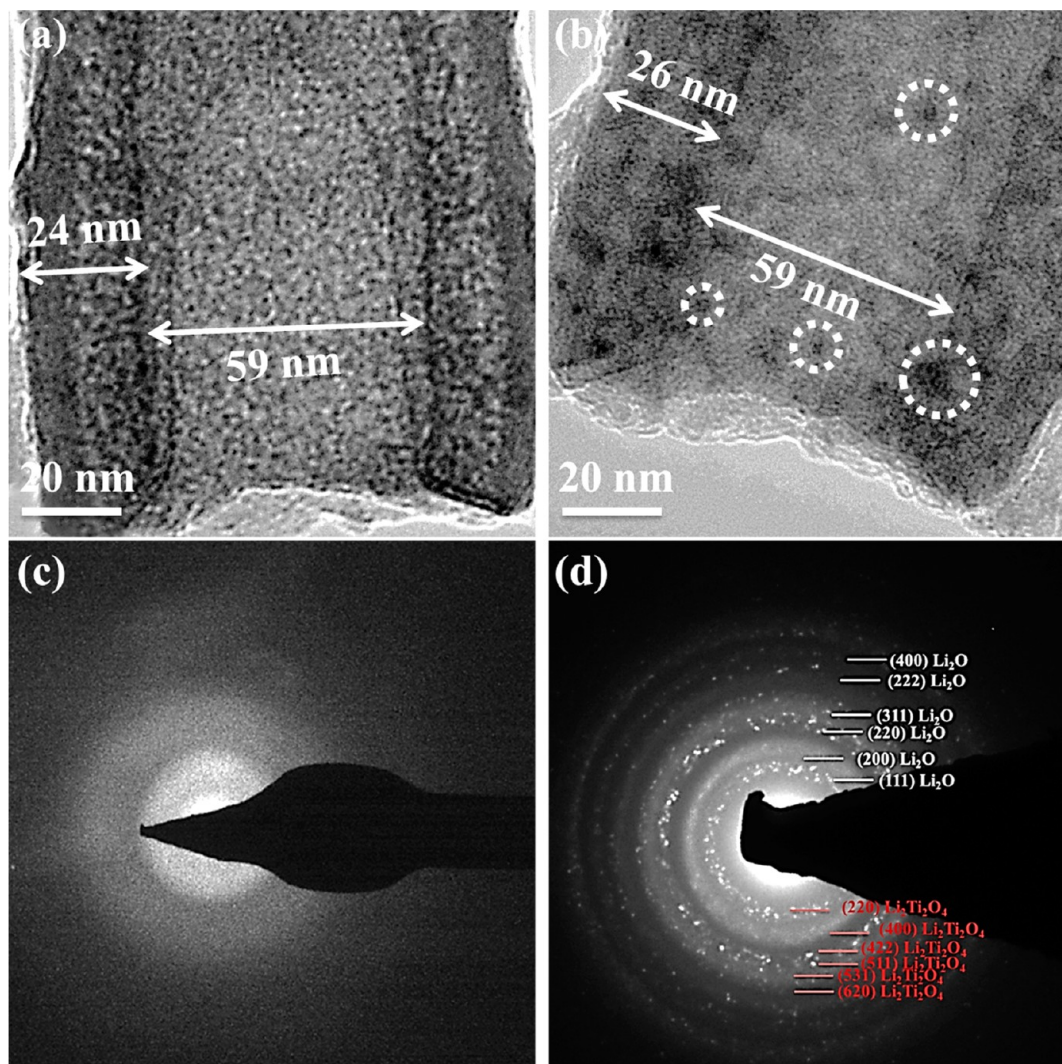


Figure 3. Bright field TEM images of an individual a-TNT (a) before lithiation and (b) after lithiation. The white arrows in (a) and (b) indicate that the wall thickness increases from ~24 to ~26 nm during lithiation, while no obvious change is seen for the nanotube inner diameter (~59 nm). Several dark contrast particles are detected in the lithiated a-TNT (marked by white dotted circles in (b)). (c, d) Corresponding SAED patterns of pristine and lithiated a-TNTs. The nanotube is demonstrated to be amorphous before lithiation in (c). The electron diffraction rings in (d) are indexed to be Li₂O and Li₂Ti₂O₄, respectively.

to form Li₂O. This situation is more likely to happen during the lithiation of intercalation materials since the rate of Li ions intercalation is limited due to the restriction in available interatomic spaces and diffusion channels. This scenario is in

synergy with the observation of Liu et al.,³⁹ who reported a similar surface Li₂O layer on the multiwall carbon nanotubes (MWCNTs), which is an intercalation material. The formation of this Li₂O layer can also be attributed to reaction of Li with

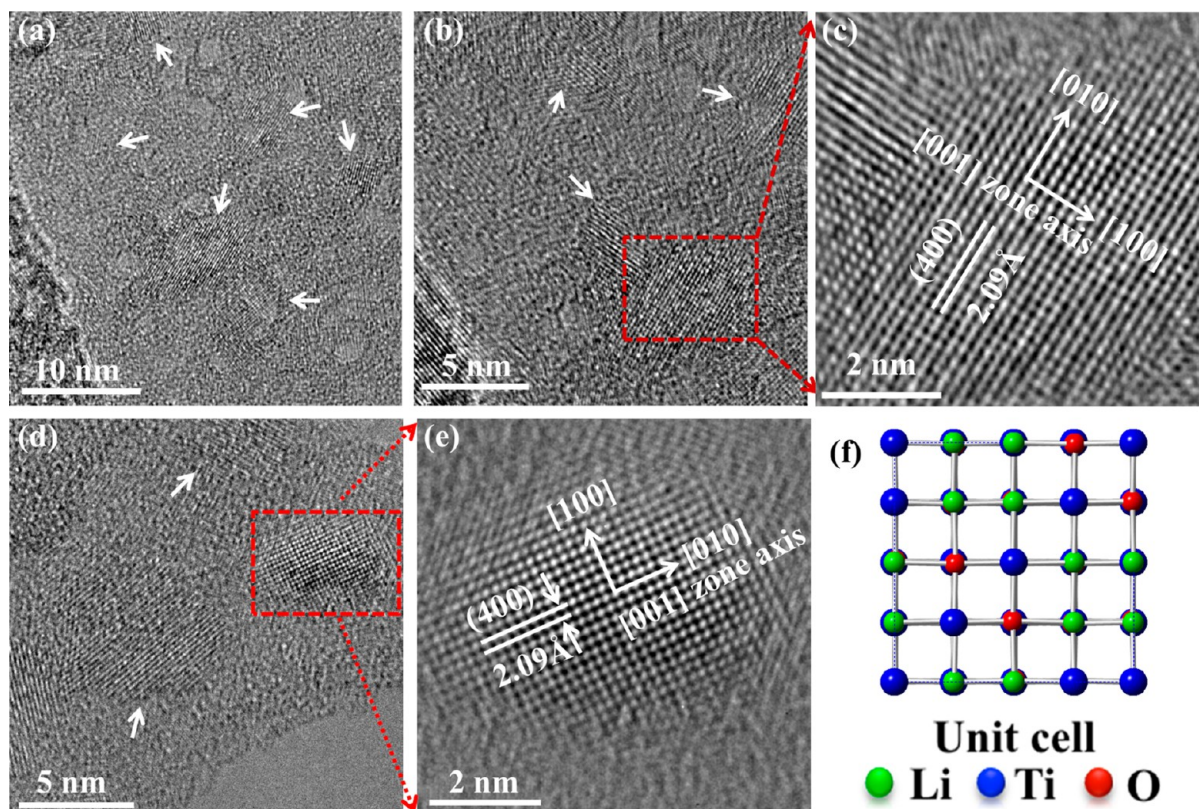


Figure 4. TEM images reveal the formation of $\text{Li}_2\text{Ti}_2\text{O}_4$ crystals within the amorphous matrix. (a) A zoom-out image of an area within lithiated amorphous TiO_2 where the presence of several crystalline particles is marked by white arrows. (b) A closer view of the crystalline particles shows the lattice fringes of crystalline particles. (c) High resolution TEM image of the particle marked by the red dotted box in (b) shows the atomic ordering within the crystalline particles. The particles are viewed along $[001]$ zone axis, and the interatomic distance of 2.09 \AA was correlated to (400) planes in $\text{Li}_2\text{Ti}_2\text{O}_4$ crystals. (d, e) The existence of the crystalline particles within the lithiated amorphous matrix was also confirmed in other locations. (f) A unit cell of the $\text{Li}_2\text{Ti}_2\text{O}_4$ crystals viewed along $[001]$ zone axis.

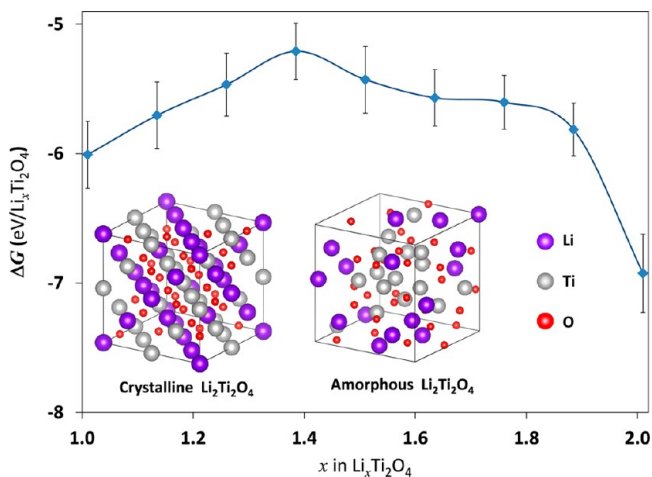


Figure 5. Difference in the Gibbs free energy for the crystalline and amorphous phases for different values of x in $\text{Li}_x\text{Ti}_2\text{O}_4$. The error bars represent the standard deviation in the energy calculations from the five amorphous samples for each value of x . Lower values of ΔG result in a stronger tendency to form a crystalline phase out of the amorphous phase. Clearly the lowest value of ΔG in this range of x is for $x = 2.00$. Also shown in the figure are the molecular structures for crystalline and amorphous DFT models. Both of the displayed structures contain 64 atoms (the crystalline image also contains periodic images).

residual oxidic groups including carboxylic acid, epoxy, or hydroxyl groups.⁴⁰ These groups can form on the surface of TiO_2 nanotubes during the electrochemical anodization process.⁴¹

In order to investigate the chemical signature change during lithiation, EELS was conducted on individual nanotubes. Figure 2a is a comparison of the EELS between the pristine and lithiated a-TNT. The Li K edge located at the energy loss position of 63.4 eV is similar to the ones in TiO_2 (rutile)⁴² and LiNiO_2 ⁴³ via the same intercalation mechanism. Another rise of the Li K edge at 58.9 and 63.4 eV closely matches that of pure Li_2O , consistently supporting the observation of Li_2O formation on the surface of the nanotube upon lithiation.

Figure 2b shows the EELS of Ti L edge in a-TNTs before and after lithiation. In the pristine nanotube, the main feature is the $2p$ spin-orbit interaction splitting into the $2p_{3/2}$ (459.1 eV) and $2p_{1/2}$ (464.5 eV) levels with a separation of 5.4 eV .^{44,45} The energy loss position of the peak is sensitive to the valence of Ti. After lithiation, these two positions of energy loss shifted toward a low energy region, indicating that the valence of Ti^{4+} reduces to Ti^{3+} to accommodate Li^+ intercalation, which is consistent with the observation from previous reports.^{46,47} More evidence is provided by the O K edges between the pristine and lithiated nanotube in Figure 2c. Prior to lithiation, the pre-edge peak (i) and main peak (ii) located on the energy loss position of 530.9 and 543.2 eV , respectively, corresponds to electron transition from $1s$ to oxygen $2p$ states hybridized with titanium $4s$ and $4p$ states.⁴² After lithiation, the energy loss

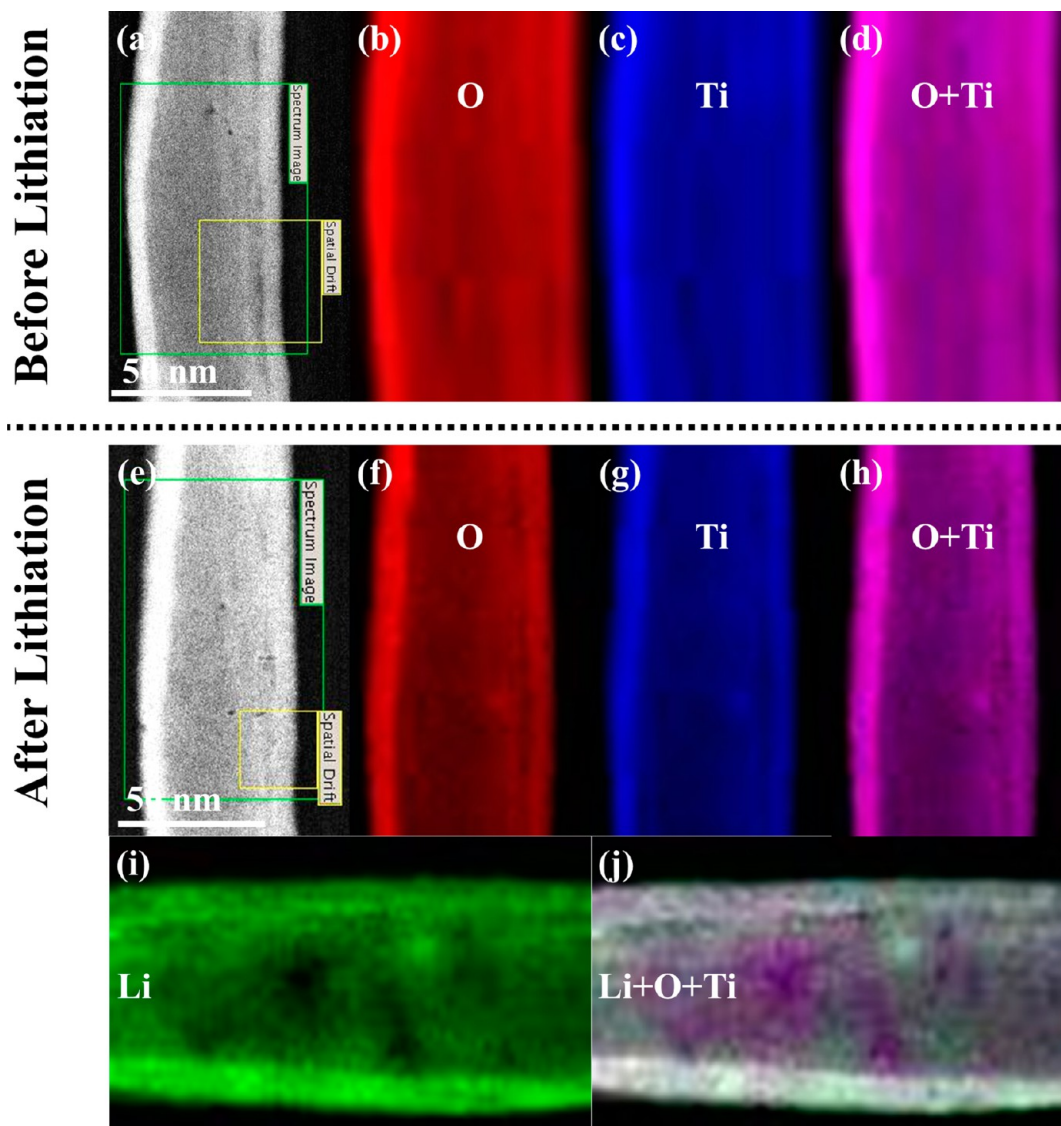


Figure 6. STEM-EELS mapping of an individual a-TNT before and after lithiation shows the chemical distribution of Ti, O, and Li in the nanotube. A selected area of EELS mapping shows the uniform distribution of O and Ti before lithiation (a–d) and after lithiation (e–h). (i) Li distribution by EELS mapping indicating the successful lithiation in the nanotube. (j) EELS mapping of Li, O, and Ti in the lithiated nanotube, showing the Li ions distributing randomly in the matrix.

position of the pre-edge peak shifted 3.1 eV to high energy loss direction as compared with the pristine nanotube. The observed shifting in the O *K* edges toward the high energy can be related to the reduction of the Ti ions following the insertion of Li into the lattice, indicating charge transfer from Li to Ti ions.⁴⁸ Another significant feature in the lithiated nanotube was the decreasing of separation between the peaks (i) and (ii). Yoshiya et al.⁴⁸ had systematically studied the structure of TiO_x ($x < 2$). They noticed that with the decrease of the x value, the separation between peaks (i) and (ii) on the O *K* edges decreased, indicating the valence reduction of Ti upon Li ions intercalation. This conclusion is closely consistent with our experimental EELS results. In addition, one can notice that, after lithiation, the intensity of peak (i) became smaller than that of peak (ii), which is due to Li_2O formation on the surface.⁴⁹

Our EELS observation is in a good agreement with the intercalation mechanism of Li ions into TiO_2 , which can be expressed as⁵⁰



In the reaction, the insertion of positively charged Li^+ is balanced with an uptake of electrons to compensate Ti^{3+} cations in the Ti^{4+} sublattice. The maximum x after charging depends on the phase structure of TiO_2 (e.g., amorphous, anatase, or rutile). The variation of x is also predicted by theoretical calculations^{51–57} and has been observed in X-ray photoelectron spectroscopy (XPS) experiments.^{58,59} Recent studies^{60–62} on the use of TiO_2 (anatase and brookite- TiO_2) nanotube anodes in a lithium battery demonstrate an initial capacity of 282 mAh/g at a specific current density of 0.24 mA/g in brookite, which corresponds to $x = 0.98$ in eq 1. For amorphous TiO_2 , associated with the disordered structures, no theoretical simulations and structural variation analysis by XRD have been conducted to calculate the maximum value of x . However, the experimental results^{11,14} show that the capacity performance of amorphous TiO_2 is better than that of anatase

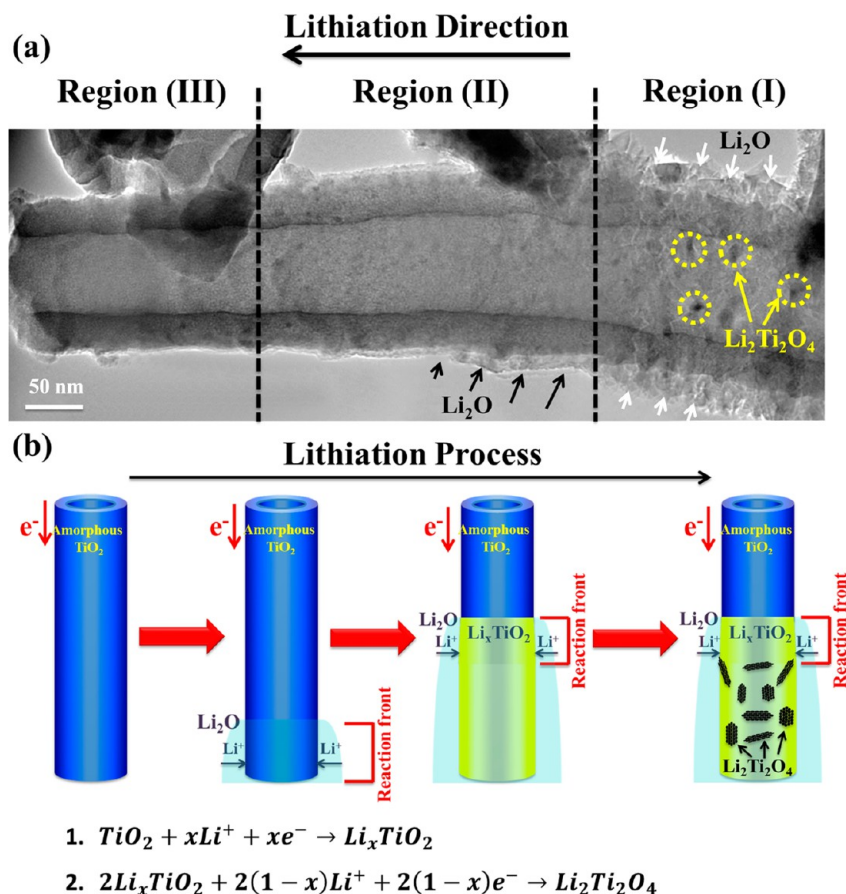


Figure 7. (a) Three distinctive regions are captured during lithiation of a single a-TNT. In region (I), the nanotube is fully lithiated as evident by the formation of polycrystalline Li_2O layer and crystalline $\text{Li}_2\text{Ti}_2\text{O}_4$ islands. In region (II), the nanotube is partially lithiated as evident by the progressive formation of Li_2O layer. No crystalline $\text{Li}_2\text{Ti}_2\text{O}_4$ islands could be detected. In region (III), the very end of the nanotube is still in the pristine state (unlithiated). (b) The schematic graph shows various stages of the lithiation process in a-TNTs.

due to more sites and defects available for Li ions insertion in amorphous TiO_2 .

A close examination of the lithiated a-TNT walls indicated that the thickness of the wall increased from ~ 24 to ~ 26 nm, which corresponded to $\sim 3.7\%$ expansion in the radial direction of the nanotube as indicated in Figure 3a,b. In fact, recent ex situ studies^{11,14,15} on a-TNTs reported a volume increase of less than 3% in fully lithiated TNTs compared with the nonlithiated ones. Due to the geometrical limitation of the in situ setup, it is very hard to directly measure the longitudinal elongation of the nanotube. However, based on the overall volume expansion calculation ($V_e/V = S_e/S \times l_e/l = d_e^2/d^2 \times l_e/l$), one can notice that the volume expansion depends on the ratios of S_e/S and l_e/l . In our study, the ratio of S_e/S is only 0.0013, which indicates that the overall volume expansion for the TiO_2 nanotube can be within 3%.

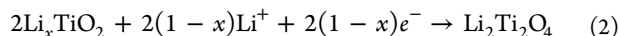
Interestingly, the inner diameter of the nanotube remained unchanged (~ 59 nm before and after lithiation) as shown in Figure 3a,b. This indicates that small radial expansion discussed earlier is mainly due to radial intercalation from the surface while no or little lithiation has happened in the depth of the nanotube. This explanation is plausible considering the poor electrical conductivity of amorphous TiO_2 . Due to this limiting factor, Li ions cannot intercalate deep into the interior structure of the nanotube. Therefore, it is expected that the lithiation is limited to the nanotube surface. This is mediated by the presence of the Li_2O layer on the surface of the TiO_2

nanotubes, which provides a convenient path for diffusion of Li ions.

The SAED pattern of the pristine nanotube shown in Figure 3c indicates an amorphous structure, as it would be expected. After lithiation, some particles with dark contrast appeared in the amorphous Li_xTiO_2 matrix as marked by white dotted circles in Figure 3b. The corresponding SAED pattern shown in Figure 3d indicates that the lithiated a-TNT is dominated by crystalline $\text{Li}_2\text{Ti}_2\text{O}_4$ and Li_2O phases as evidenced by matching the experimental electron diffraction rings with the calculated pattern based on the $\text{Li}_2\text{Ti}_2\text{O}_4$ (space group: $Fm3m$, lattice constants: $a = b = c = 8.375$ Å)⁶³ and Li_2O structure, respectively.

To better understand the nature of the dark contrast particles, HRTEM imaging was performed on the lithiated nanotube. Figure 4 shows HRTEM analysis of the particles at two different locations of the same lithiated nanotube. Figure 4a shows that some crystalline particles (marked by white arrows) are distributed almost randomly within the amorphous matrix. A closer view enables one to observe the lattice fringes in the particles, indicating the presence of atomic ordering in the amorphous matrix. The HRTEM image of one of the particles with the $[001]$ zone axis is shown in Figure 4c. The HRTEM image shows the well-defined (400) crystal planes with the spacing of 2.09 Å, confirming the formation of the crystalline $\text{Li}_2\text{Ti}_2\text{O}_4$ phase. Figure 4d,e confirms the presence of similar crystals at other locations in the amorphous matrix. Therefore,

the Reaction 1 can be modified to include the new crystalline phase according to



The in situ observation of crystalline $\text{Li}_2\text{Ti}_2\text{O}_4$ formation in amorphous TiO_2 is the first direct evidence of such a phenomenon in TiO_2 anodes and is in agreement with the recent ex situ electrochemical studies. Using synchrotron X-ray diffraction, Xiong et al.⁶⁴ reported the evidence for an electrochemically driven transformation of amorphous TiO_2 nanotubes into a crystalline phase that self-improved as the cycling proceeded. The adopted cubic structure showed long-term reversibility and enhanced power with capacity approaching the stoichiometry of $\text{Li}_2\text{Ti}_2\text{O}_4$. Using XRD, Ryu et al.⁶⁵ reported that the irreversible Li capacity observed in the amorphous TiO_2 nanotube was primarily due to the formation of crystalline Li_xTiO_2 , which was assumed to be an inactive phase. On the basis of such evidence, one can conclude that the exposure of amorphous TiO_2 to the electron beam is not the driving force for the formation of crystalline $\text{Li}_2\text{Ti}_2\text{O}_4$. In fact, the close agreement between in situ TEM studies of battery reactions and ex situ electrochemistry results is well supported in the literature.^{22,28}

It is expected that the continuous lithiation of Li_xTiO_2 will lead to an atomic rearrangement in the amorphous Li_xTiO_2 matrix to form crystals of $\text{Li}_2\text{Ti}_2\text{O}_4$ with the $\text{Li}:\text{TiO}_2$ stoichiometry of 1. To verify this, a series of DFT simulations were conducted to demonstrate the strong tendency of $\text{Li}_2\text{Ti}_2\text{O}_4$ to transform from the amorphous to crystalline structure relative to $\text{Li}_x\text{Ti}_2\text{O}_4$ where $1.0 \leq x < 2$. DFT models were developed for crystalline and amorphous structures for $x = 1.00, 1.13, 1.25, 1.38, 1.50, 1.63, 1.75, 1.88, \text{ and } 2.00$. Five independent samples of the amorphous structures were established for each value of x for statistical relevancy. Further details of these calculations are described in the Supporting Information. Figure 5 shows the simulated structure for crystalline $\text{Li}_2\text{Ti}_2\text{O}_4$ and a representative structure for amorphous $\text{Li}_2\text{Ti}_2\text{O}_4$. The internal energy of formation for $\text{Li}_x\text{Ti}_2\text{O}_4$ was calculated as

$$U_f(x) = U_{\text{Li}_x\text{Ti}_2\text{O}_4} - xU_{\text{Li}} - U_{\text{Ti}_2\text{O}_4}$$

where $U_{\text{Li}_x\text{Ti}_2\text{O}_4}$ is the electronic energy of $\text{Li}_x\text{Ti}_2\text{O}_4$, x is the number of Li atoms per Ti_2O_4 , U_{Li} is the energy of a single Li atom in a BCC Li crystal, and $U_{\text{Ti}_2\text{O}_4}$ is the energy of Ti_2O_4 (rutile crystal structure). The driving force for crystallization is the difference in the Gibbs free energy between the crystalline and amorphous phases, which is given by

$$\Delta G = G_{\text{crystalline}} - G_{\text{amorphous}}$$

Because the temperatures and pressures of the DFT simulations were 0 K and 0 atm, respectively, the change in Gibbs free energy is

$$\Delta G = U_{\text{crystalline}} - U_{\text{amorphous}}$$

where $U_{\text{crystalline}}$ and $U_{\text{amorphous}}$ are the internal energies of formation for the crystalline and amorphous states, respectively. A plot of the Gibbs free energy is shown in Figure 5. From the plot it is clear that the largest driving force for crystallization is at $x = 2$. Therefore, there is a significantly higher probability of formation of $\text{Li}_2\text{Ti}_2\text{O}_4$ crystalline phases relative to $\text{Li}_x\text{Ti}_2\text{O}_4$ with $1 \leq x < 2$ during the lithiation process.

These simulation results are in agreement with the results of molecular dynamics simulations of Xiong et al.,⁶⁴ where the formation of $\text{Li}_2\text{Ti}_2\text{O}_4$ in a-TNTs after lithiation was predicted. Their simulation results revealed that at high lithiation levels (>75%) the atomic diffusion of Ti and O became significant, suggesting facile rearrangement of atoms in the structure and leading to crystalline phase formation. They further reported that, with increasing simulation time, the Ti, O, and Li atoms would present long-range order throughout the cubic structure.⁶⁶

The size of the crystalline islands shown in Figure 4c,e provides a characteristic length scale (~ 5 nm) at which the atomic bonding configuration has been changed within a short time period. One also could note that the crystalline particles are embedded within the amorphous matrix. This can be indicative of inhomogeneous chemical changes in the amorphous matrix. More spectroscopy was conducted to capture the local chemical distributions before and after the amorphous to crystalline phase transition. Figure 6 compares the chemical distribution of a nanotube before and after lithiation by STEM-EELS elemental mapping. The EELS mapping was conducted on the same area as shown in Figure 6a,e. The elemental mapping in Figure 6b–d,f–h indicates that the chemical distribution of Ti and O elements is uniform before and after lithiation. However, the Li element mapping shown in Figure 6i demonstrates that the Li elements are distributed nonuniformly in the nanotube. For better clarity, all the maps related to Li, O, and Ti atoms are superimposed in Figure 6j, which further indicates the local changes in the chemical composition. The fluctuation of Li ions can promote the heterogeneous nucleation of the $\text{Li}_2\text{Ti}_2\text{O}_4$ crystalline phase in the amorphous matrix, which is consistent with our HRTEM observation.

It is interesting to note that the crystallization of $\text{Li}_2\text{Ti}_2\text{O}_4$ from amorphous Li_xTiO_2 is different from the $\text{Li}_{3.75}\text{Si}$ crystallization phenomenon that has been reported in Si based anode materials during lithiation.^{67–69} Recently, Gu et al.⁷⁰ revealed the mechanism of the crystallization of $\text{Li}_{15}\text{Si}_4$ from amorphous $\text{Li}_{3.75}\text{Si}$, which involved a congruent process with constant chemical composition. The transformation did not require long-range diffusion but only simple local rearrangement of atomic configurations.⁷¹ However, the crystallization of $\text{Li}_2\text{Ti}_2\text{O}_4$ from amorphous Li_xTiO_2 is a classic nucleation and growth process for which local chemical composition fluctuations lead to phase separation.

The overall lithiation mechanism of the a-TNTs is captured in Figure 7a and schematically represented in Figure 7b. Fully lithiated, partially lithiated, and unlithiated regions of the a-TNT are marked in Figure 7a. In the fully lithiated region (Region I), a thick polycrystalline Li_2O layer (marked by white arrows) is formed on the surface of the nanotube, and crystalline $\text{Li}_2\text{Ti}_2\text{O}_4$ islands are formed in the amorphous Li_xTiO_2 matrix (marked by yellow dotted circles). In Region II, only evidence of Li_2O layer can be found which indicates that some lithiation of the matrix in the form of Li_xTiO_2 could have happened. The Li_2O layer on the surface (marked by black arrows) becomes thinner as it progresses toward the unlithiated region (Region III), which means that the lithiation proceeds through the Li_2O layer. No obvious crystalline islands were detected in Region II. In the unlithiated region (Region III), the nanotube is in an amorphous state with no indication of lithiation.

On the basis of the results discussed above, a schematic design is proposed to illustrate the overall lithiation process of a-TNTs as shown in Figure 7b. The Li ions will intercalate into the nanotube by donating electrons to Ti to form Li_xTiO_2 , associating a Li_2O layer formation on the surface of the nanotube. With increasing the concentration of Li ions in the nanotube, the diffusion of O and Ti atoms will also increase⁶⁶ enabling the facile rearrangement of disordered atoms to $\text{Li}_2\text{Ti}_2\text{O}_4$ islands with crystalline structures.

The readers should also note that the in situ results discussed here do not consider the effect of electrolytes and solid electrolyte interphase (SEI) as typically observed in Li ion batteries.⁷² However, we believe that the phase Li-induced phase transitions are comparable with ex situ electrochemical cells.²² In fact, over the past few years, in situ TEM studies of lithium ion batteries carried out based on the open cell have provided important fundamental insight in the reaction kinetics and microstructural evolution during battery operations by real time observation. For example, a recently developed “operando” TEM electrochemical liquid cell consisting of the configuration of a real battery with a relevant liquid electrolyte indicated that the structural and chemical evolutions of the Si nanowire from both open cell design and closed cell designs are similar except for the formation of a thick SEI layer on the nanowire.⁷³ Liu et al. reported an anisotropic swelling of Si nanowires during lithiation by using open cell inside the TEM.²⁶ Almost at the same time, the anisotropic lithiation of Si nanopillars and microslabs were successively reported by other groups using ex situ experiments based on real Li-ion batteries.^{74,75} The studies on the structural change of Ge nanowire during lithiation/delithiation also indicate the high consistency between the in situ and ex situ TEM studies, although the experimental conditions between the two techniques differ considerably. Both techniques proved the nanopore formation in Ge nanowires during delithiation.^{32,76} This consistency shows that the electrochemical–mechanical responses observed in in situ TEM are intrinsic to the electrode materials. Thus, the information gained from the present in situ TEM studies on TiO_2 nanotubes is applicable to the design of next generation lithium ion batteries.

CONCLUSION

In summary, the electrochemical lithiation mechanism of amorphous TiO_2 nanotubes was modified based on our in situ TEM observation. Initially, Li ion movements are facilitated by the surface diffusion through the Li_2O layer at the surface of TiO_2 nanotubes. Through the surface, Li ions intercalate into the nanotubes to form an amorphous Li_xTiO_2 matrix. With the increase of Li ion concentration in the lithiated nanotube, the phase transformation from amorphous to crystalline by atomic rearrangement occurs. This leads to the formation of crystalline islands of $\text{Li}_2\text{Ti}_2\text{O}_4$ with a cubic structure in the amorphous Li_xTiO_2 matrix. This phase transformation is associated with local inhomogeneities in the Li distribution. In addition to the evidence of lithium-induced atomic ordering in amorphous TiO_2 materials, the present work provides a new reaction mechanism, supported by direct chemical and structural analyses, for the lithiation behavior of amorphous TiO_2 nanotubes.

ASSOCIATED CONTENT

Supporting Information

Details of DFT analysis and the movie of the amorphous TiO_2 nanotube lithiation process. This material is available free of charge via the Internet at <http://pubs.acs.org>.

AUTHOR INFORMATION

Corresponding Authors

*E-mail: chongmin.wang@pnnl.gov (C.W.).

*E-mail: reza@mtu.edu (R.S.-Y.).

Author Contributions

[†]These authors contributed equally (Q.G., M.G., and A.N.).

Notes

The authors declare no competing financial interest.

ACKNOWLEDGMENTS

R.S.-Y. acknowledges the financial support from the National Science Foundation (Award No. CMMI-1200383) and the American Chemical Society-Petroleum Research Fund (Award No. 51458-ND10). The acquisition of the UIC JEOL JEM-ARM200CF is supported by an MRI-R2 grant from the National Science Foundation (Grant No. DMR-0959470). G.M.O. would like to acknowledge the use of SUPERIOR, a high-performance computing cluster at Michigan Technological University. The use of the aberration-corrected electron microscope (ARM 200CF) at the UIC Electron Microscopy Service (EMS) is also acknowledged. M.G. and C.M.W. acknowledge the support of Chemical Imaging Initiative at Pacific Northwest National Laboratory (PNNL). It was conducted under the Laboratory Directed Research and Development Program at PNNL, a multiprogram national laboratory operated by Battelle under Contract DE-AC05-76RLO1830 for the U.S. Department of Energy (DOE). The work was conducted in the William R. Wiley Environmental Molecular Sciences Laboratory (EMSL), a national scientific user facility sponsored by DOE's Office of Biological and Environmental Research and located at PNNL.

REFERENCES

- (1) Amine, K.; Belharouak, I.; Chen, Z. H.; Tran, T.; Yumoto, H.; Ota, N.; Myung, S. T.; Sun, Y. K. *Adv. Mater.* **2010**, *22*, 3052–3057.
- (2) Zhou, H. S.; Wang, Y. G.; Li, H. Q.; He, P. *ChemSusChem* **2010**, *3*, 1009–1019.
- (3) Abraham, K. M. *Electrochim. Acta* **1993**, *38*, 1233–1248.
- (4) Winter, M.; Besenhard, J. O.; Spahr, M. E.; Novak, P. *Adv. Mater.* **1998**, *10*, 725–763.
- (5) Rom, I.; Wachtler, M.; Papst, I.; Schmied, M.; Besenhard, J. O.; Hofer, F.; Winter, M. *Solid State Ionics* **2001**, *143*, 329–336.
- (6) Du, N.; Zhang, H.; Chen, B.; Wu, J. B.; Ma, X. Y.; Liu, Z. H.; Zhang, Y. Q.; Yang, D.; Huang, X. H.; Tu, J. P. *Adv. Mater.* **2007**, *19*, 4505–+.
- (7) Chan, C. K.; Zhang, X. F.; Cui, Y. *Nano Lett.* **2007**, *8*, 307–309.
- (8) Jansen, A. N.; Kahaian, A. J.; Kepler, K. D.; Nelson, P. A.; Amine, K.; Dees, D. W.; Vissers, D. R.; Thackeray, M. M. *J. Power Sources* **1999**, *81*, 902–905.
- (9) Fu, L. J.; Liu, H.; Zhang, H. P.; Li, C.; Zhang, T.; Wu, Y. P.; Holze, R.; Wu, H. Q. *Electrochem. Commun.* **2006**, *8*, 1–4.
- (10) Wagemaker, M.; Kearley, G. J.; van Well, A. A.; Mutka, H.; Mulder, F. M. *J. Am. Chem. Soc.* **2003**, *125*, 840–848.
- (11) Ortiz, G. F.; Hanzu, I.; Djenizian, T.; Lavela, P.; Tirado, J. L.; Knauth, P. *Chem. Mater.* **2009**, *21*, 63–67.
- (12) Jin, B.; Gu, H.-B.; Kim, K.-W. *J. Solid State Electrochem.* **2008**, *12*, 105–111.

- (13) Strobel, P.; Tillier, J.; Diaz, A.; Ibarra-Palos, A.; Thiéry, F.; Soupart, J. B. *J. Power Sources* **2007**, *174*, 910–915.
- (14) Guan, D.; Cai, C.; Wang, Y. *J. Nanosci. Nanotechnol.* **2011**, *11*, 3641–3650.
- (15) Wei, Z.; Liu, Z.; Jiang, R.; Bian, C.; Huang, T.; Yu, A. *J. Solid State Electrochem.* **2010**, *14*, 1045–1050.
- (16) Fang, H. T.; Liu, M.; Wang, D. W.; Sun, T.; Guan, D. S.; Li, F.; Zhou, J.; Sham, T. K.; Cheng, H. M. *Nanotechnology* **2009**, *20*, 225701.
- (17) Bi, Z.; Paranthaman, M. P.; Menchhofer, P. A.; Dehoff, R. R.; Bridges, C. A.; Chi, M.; Guo, B.; Sun, X.-G.; Dai, S. *J. Power Sources* **2013**, *222*, 461–466.
- (18) González, J. R.; Alcántara, R.; Nacimient, F.; Ortiz, G. F.; Tirado, J. L.; Zhecheva, E.; Stoyanova, R. *J. Phys. Chem. C* **2012**, *116*, 20182–20190.
- (19) Borghols, W. J. H.; Lützenkirchen-Hecht, D.; Haake, U.; Chan, W.; Lafont, U.; Kelder, E. M.; van Eck, E. R. H.; Kentgens, A. P. M.; Mulder, F. M.; Wagemaker, M. *J. Electrochem. Soc.* **2010**, *157*, A582–A588.
- (20) Wang, C. M.; Xu, W.; Liu, J.; Choi, D. W.; Arey, B.; Saraf, L. V.; Zhang, J. G.; Yang, Z. G.; Thevuthasan, S.; Baer, D. R.; Salmon, N. J. *Mater. Res.* **2010**, *25*, 1541–1547.
- (21) Huang, J. Y.; Zhong, L.; Wang, C. M.; Sullivan, J. P.; Xu, W.; Zhang, L. Q.; Mao, S. X.; Hudak, N. S.; Liu, X. H.; Subramanian, A.; Fan, H.; Qi, L.; Kushima, A.; Li, J. *Science* **2010**, *330*, 1515–1520.
- (22) Ghassemi, H.; Au, M.; Chen, N.; Heiden, P. A.; Yassar, R. S. *ACS Nano* **2011**, *5*, 7805–7811.
- (23) Ghassemi, H.; Au, M.; Chen, N.; Heiden, P. A.; Yassar, R. S. *Appl. Phys. Lett.* **2011**, *99*, 123113.
- (24) Gu, M.; Li, Y.; Li, X.; Hu, S.; Zhang, X.; Xu, W.; Thevuthasan, S.; Baer, D. R.; Zhang, J.-G.; Liu, J.; Wang, C. *ACS Nano* **2012**, *6*, 8439–8447.
- (25) Nie, A.; Gan, L.-Y.; Cheng, Y.; Asayesh-Ardakani, H.; Li, Q.; Dong, C.; Tao, R.; Mashayek, F.; Wang, H.-T.; Schwingenschlögl, U.; Klie, R. F.; Yassar, R. S. *ACS Nano* **2013**, *7*, 6203–6211.
- (26) Liu, X. H.; Zhang, L. Q.; Zhong, L.; Liu, Y.; Zheng, H.; Wang, J. W.; Cho, J.-H.; Dayeh, S. A.; Picraux, S. T.; Sullivan, J. P.; Mao, S. X.; Ye, Z. Z.; Huang, J. Y. *Nano Lett.* **2011**, *11*, 2251–2258.
- (27) Wang, C.-M.; Li, X.; Wang, Z.; Xu, W.; Liu, J.; Gao, F.; Kovarik, L.; Zhang, J.-G.; Howe, J.; Burton, D. J.; Liu, Z.; Xiao, X.; Thevuthasan, S.; Baer, D. R. *Nano Lett.* **2012**, *12*, 1624–1632.
- (28) Yang, H.; Huang, S.; Huang, X.; Fan, F.; Liang, W.; Liu, X. H.; Chen, L.-Q.; Huang, J. Y.; Li, J.; Zhu, T.; Zhang, S. *Nano Lett.* **2012**, *12*, 1953–1958.
- (29) Liu, X. H.; Zhong, L.; Huang, S.; Mao, S. X.; Zhu, T.; Huang, J. Y. *ACS Nano* **2012**, *6*, 1522–1531.
- (30) Liu, X. H.; Wang, J. W.; Huang, S.; Fan, F.; Huang, X.; Liu, Y.; Krylyuk, S.; Yoo, J.; Dayeh, S. A.; Davydov, A. V.; Mao, S. X.; Picraux, S. T.; Zhang, S.; Li, J.; Zhu, T.; Huang, J. Y. *Nat. Nanotechnol.* **2012**, *7*, 749–756.
- (31) McDowell, M. T.; Ryu, I.; Lee, S. W.; Wang, C.; Nix, W. D.; Cui, Y. *Adv. Mater.* **2012**, *24*, 6034–6041.
- (32) Liu, X. H.; Huang, S.; Picraux, S. T.; Li, J.; Zhu, T.; Huang, J. Y. *Nano Lett.* **2011**, *11*, 3991–3997.
- (33) Liu, Y.; Hudak, N. S.; Huber, D. L.; Limmer, S. J.; Sullivan, J. P.; Huang, J. Y. *Nano Lett.* **2011**, *11*, 4188–4194.
- (34) Wang, C.-M.; Xu, W.; Liu, J.; Zhang, J.-G.; Saraf, L. V.; Arey, B. W.; Choi, D.; Yang, Z.-G.; Xiao, J.; Thevuthasan, S.; Baer, D. R. *Nano Lett.* **2011**, *11*, 1874–1880.
- (35) Zhang, L. Q.; Liu, X. H.; Perng, Y.-C.; Cho, J.; Chang, J. P.; Mao, S. X.; Ye, Z. Z.; Huang, J. Y. *Micron* **2012**, *43*, 1127–1133.
- (36) Zhong, L.; Liu, X. H.; Wang, G. F.; Mao, S. X.; Huang, J. Y. *Phys. Rev. Lett.* **2011**, *106*, 248302.
- (37) Kushima, A.; Liu, X. H.; Zhu, G.; Wang, Z. L.; Huang, J. Y.; Li, J. *Nano Lett.* **2011**, *11*, 4535–4541.
- (38) Liu, X. H.; Wang, J. W.; Liu, Y.; Zheng, H.; Kushima, A.; Huang, S.; Zhu, T.; Mao, S. X.; Li, J.; Zhang, S.; Lu, W.; Tour, J. M.; Huang, J. Y. *Carbon* **2012**, *50*, 3836–3844.
- (39) Liu, Y.; Zheng, H.; Liu, X. H.; Huang, S.; Zhu, T.; Wang, J.; Kushima, A.; Hudak, N. S.; Huang, X.; Zhang, S.; Mao, S. X.; Qian, X.; Li, J.; Huang, J. Y. *ACS Nano* **2011**, *5*, 7245–7253.
- (40) Su, Q.; Chang, L.; Zhang, J.; Du, G.; Xu, B. *J. Phys. Chem. C* **2013**, *117*, 4292–4298.
- (41) Shin, D. H.; Shokuhfar, T.; Choi, C. K.; Lee, S.-H.; Friedrich, C. *Nanotechnology* **2011**, *22*, 315704.
- (42) Wang, C. M.; Yang, Z. G.; Thevuthasan, S.; Liu, J.; Baer, D. R.; Choi, D.; Wang, D. H.; Zhang, J. G.; Saraf, L. V.; Nie, Z. M. *Appl. Phys. Lett.* **2009**, *94*, 233116.
- (43) Koyama, Y.; Mizoguchi, T.; Ikeno, H.; Tanaka, I. *J. Phys. Chem. B* **2005**, *109*, 10749–10755.
- (44) Okada, M.; Jin, P.; Yamada, Y.; Tazawa, M.; Yoshimura, K. *Surf. Sci.* **2004**, *566–568* (Part 2), 1030–1034.
- (45) Bertoni, G.; Beyers, E.; Verbeeck, J.; Mertens, M.; Cool, P.; Vansant, E. F.; Van Tendeloo, G. *Ultramicroscopy* **2006**, *106*, 630–635.
- (46) Lusvardi, V. S.; Barteau, M. A.; Chen, J. G.; Eng, J., Jr.; Fröhberger, B.; Teplyakov, A. *Surf. Sci.* **1998**, *397*, 237–250.
- (47) Akita, T.; Okumura, M.; Tanaka, K.; Ohkuma, K.; Kohyama, M.; Koyanagi, T.; Date, M.; Tsubota, S.; Haruta, M. *Surf. Interface Anal.* **2005**, *37*, 265–269.
- (48) Yoshiya, M.; Tanaka, I.; Kaneko, K.; Adachi, H. *J. Phys.: Condens. Matter* **1999**, *11*, 3217.
- (49) Zheng, H.; Liu, Y.; Mao, S. X.; Wang, J.; Huang, J. Y. *Sci. Rep.* **2012**, *2*.
- (50) Van De Krol, R.; Goossens, A.; Schoonman, J. *J. Phys. Chem. B* **1999**, *103*, 7151–7159.
- (51) Olson, C. L.; Nelson, J.; Islam, M. S. *J. Phys. Chem. B* **2006**, *110*, 9995–10001.
- (52) Stashans, A.; Lunell, S.; Bergstroem, R.; Hagfeldt, A.; Lindquist, S.-E. *Phys. Rev. B: Condens. Matter* **1996**, *53*, 159.
- (53) Mackrodt, W. C. *J. Solid State Chem.* **1999**, *142*, 428–439.
- (54) Koudriachova, M. V.; de Leeuw, S. W.; Harrison, N. M. *Phys. Rev. B* **2004**, *69*, 054106.
- (55) Koudriachova, M. V.; de Leeuw, S. W.; Harrison, N. M. *Phys. Rev. B* **2004**, *70*, 165421.
- (56) Koudriachova, M. V.; Harrison, N. M.; de Leeuw, S. W. *Phys. Rev. B: Condens. Matter* **2002**, *65*, 235423.
- (57) Muscat, J.; Swamy, V.; Harrison, N. M. *Phys. Rev. B* **2002**, *65*, 224112.
- (58) Sodergren, S.; Siegbahn, H.; Rensmo, H.; Lindstrom, H.; Hagfeldt, A.; Lindquist, S.-E. *J. Phys. Chem. B* **1997**, *101*, 3087–3090.
- (59) Henningsson, A.; Rensmo, H.; Sandell, A.; Siegbahn, H.; Sodergren, S.; Lindstrom, H.; Hagfeldt, A. *J. Chem. Phys.* **2003**, *118*, 5607–5612.
- (60) Li, J.; Tang, Z.; Zhang, Z. *Electrochem. Commun.* **2005**, *7*, 62–67.
- (61) Zhou, Y. K.; Cao, L.; Zhang, F.-b.; He, B.-l.; Li, H.-l. *J. Electrochem. Soc.* **2003**, *150*, A1246–A1249.
- (62) Armstrong, G.; Armstrong, A. R.; Canales, J.; Bruce, P. G. *Chem. Commun.* **2005**, 2454–2456.
- (63) Cava, R. J.; Murphy, D. W.; Zahurak, S.; Santoro, A.; Roth, R. S. *J. Solid State Chem.* **1984**, *53*, 64–75.
- (64) Xiong, H.; Yildirim, H.; Shevchenko, E. V.; Prakapenka, V. B.; Koo, B.; Slater, M. D.; Balasubramanian, M.; Sankaranarayanan, S. K. R. S.; Greeley, J. P.; Tepavcevic, S.; Dimitrijevic, N. M.; Podsiadlo, P.; Johnson, C. S.; Rajh, T. *J. Phys. Chem. C* **2011**, *116*, 3181–3187.
- (65) Ryu, W.-H.; Nam, D.-H.; Ko, Y.-S.; Kim, R.-H.; Kwon, H.-S. *Electrochim. Acta* **2012**, *61*, 19–24.
- (66) Yildirim, H.; Greeley, J. P.; Sankaranarayanan, S. K. R. S. *J. Phys. Chem. C* **2013**, *117*, 3834–3845.
- (67) Kim, H.; Kweon, K. E.; Chou, C.-Y.; Ekerdt, J. G.; Hwang, G. S. *J. Phys. Chem. C* **2010**, *114*, 17942–17946.
- (68) Zhang, Q.; Zhang, W.; Wan, W.; Cui, Y.; Wang, E. *Nano Lett.* **2010**, *10*, 3243–3249.
- (69) Zhang, Q.; Cui, Y.; Wang, E. *J. Phys. Chem. C* **2011**, *115*, 9376–9381.
- (70) Gu, M.; Wang, Z.; Connell, J. G.; Perea, D. E.; Lauhon, L. J.; Gao, F.; Wang, C. *ACS Nano* **2013**, *7*, 6303–6309.
- (71) Zubarev, E. N. *Phys.-Usp.* **2011**, *54*, 473.

(72) Verma, P.; Maire, P.; Novák, P. *Electrochim. Acta* **2010**, *55*, 6332–6341.

(73) Gu, M.; Parent, L. R.; Mehdi, B. L.; Unocic, R. R.; McDowell, M. T.; Sacci, R. L.; Xu, W.; Connell, J. G.; Xu, P.; Abellan, P.; Chen, X.; Zhang, Y.; Perea, D. E.; Evans, J. E.; Lauhon, L. J.; Zhang, J.-G.; Liu, J.; Browning, N. D.; Cui, Y.; Arslan, I.; Wang, C.-M. *Nano Lett.* **2013**, *13*, 6106–6112.

(74) Lee, S. W.; McDowell, M. T.; Choi, J. W.; Cui, Y. *Nano Lett.* **2011**, *11*, 3034–3039.

(75) Goldman, J. L.; Long, B. R.; Gewirth, A. A.; Nuzzo, R. G. *Adv. Funct. Mater.* **2011**, *21*, 2412–2422.

(76) Park, M.-H.; Cho, Y.; Kim, K.; Kim, J.; Liu, M.; Cho, J. *Angew. Chem., Int. Ed.* **2011**, *50*, 9647–9650.